

Spatio temporal characterization of interfacial Faraday waves: A new absorption technique

A.V. Kityk

*Institute for Computer Science, Technical University of Czestochowa,
Electrical Eng. Dep., Al. Armii Krajowej 17, PL-42200 Czestochowa, Poland*

J.Embs, V. V. Mekhonoshin

Theoretische Physik, Universität des Saarlandes, 66041 Saarbrücken, Germany

C. Wagner*

Experimentalphysik, Universität des Saarlandes, 66041 Saarbrücken, Germany

(Dated: September 26, 2018)

We present measurements of the complete spatio-temporal Fourier spectrum of Faraday waves. The Faraday waves are generated at the interface of two immiscible index matched liquids of different density. By use of a new absorption technique we are able to determine the bifurcation scenario from the flat surface to the patterned state for each complex spatial and temporal Fourier component separately. The measured surface spectra at onset are in good agreement with the predictions from a linear stability analysis. For the nonlinear state our measurements show in a direct manner how energy is transferred from lower to higher harmonics and we quantify the nonlinear coupling coefficients. Furthermore we find that the nonlinear coupling generates constant components in the spatial Fourier spectrum leading to a contribution of a non oscillating permanent sinusoidal deformed surface state. A comparison of a hexagonal and a rectangular pattern reveals that spatial resonances only can give rise to a spectrum that violates the temporal resonance conditions given by the weakly nonlinear theory.

PACS numbers: 89.75.Kd, 47.54.+r, 47.35.+i, 47.20.Gv

1. Introduction

The Faraday Experiment is probably the first non equilibrium pattern forming system that has been investigated scientifically, namely by Michael Faraday in 1831 [1]. Nevertheless it was only recently that it was possible to determine the complete Fourier spectrum of the deformed surface state [2]. While an experimental analysis of the full mode spectrum in other pattern forming model systems like Rayleigh-Benard or Taylor-Couette has been standard technique for a long time, it is the refraction of light at the free surface of a liquid that renders the analysis of surface waves so difficult. Quantitative information about the patterned state up to higher orders is important not only to verify the validity of theoretical calculations [3, 4] but also to gain insight on the resonance mechanisms that *form* the patterns. The Faraday experiment is especially known for its richness of different patterns that are observed [5, 6, 7, 8, 9, 10]. By using complex liquids [11], very low fill heights [12] or by introducing additional driving frequencies, highly complex ordered states like superlattices [13, 14] have been observed recently. But we will demonstrate that even simple patterns like lines, squares and hexagons observed in a single driving frequency experiment can still unveil unknown surprising characteristics.

A discussion of the different attempts to reveal quantitative information on the the surface elevation profile $\zeta(r, t)$ of Faraday waves is given in [15]. The main difficulties in determining the surface elevation profile of capillary waves at the the free surface are the difference in refractive indexes of the liquid and the air, and the fact that the interface diffuses almost no light but rather reflects or transmits incoming light completely. To our knowledge there is only one optical method that overcomes this problem with the use Polystyrene colloids to provide light scatterers within the fluid [17], but the method was only used in a turbulent regime. Another powerful method for the investigation of capillary waves on ferrofluids based on x-ray absorption was presented in [16], but the related costs and efforts might be justified for fully opaque liquids only. To bypass the problems associated with light refraction and reflection on a liquid-air interface we chose to study the interface between two index matched liquids. The upper fluid is transparent, the lower one is dyed. In the presence of surface deformations the instantaneous thickness can be deduced from the intensity of the light transmitted trough the colored layer. From a hydrodynamic point of view the replacement of the air by a second liquid is nothing but a change of viscosity and density, though the low kinematic viscosity of air simplifies the theoretical calculations. However, the first exact theoretical analysis of the linear stability problem by Kumar and Tuckerman [3] was carried out for the more general case of a system of two layers of liquid.

*Electronic address: c.wagner@mx.uni-saarland.de

2. Experimental setup

The experimental setup is shown in Fig. 1. The container consists of an aluminium ring (diameter $D = 18$ cm) separating two parallel glass windows by a gap of 10 mm. It is filled by two unmixible liquids: a silicone oil (SOIL, Dow Corning, viscosity $\eta = 20$ mPas, density $\rho = 949$ kg/m³) and an aqueous solution of sugar and NiSO₄ (WSS, $\eta = 7.2$ mPas, $\rho = 1185$ kg/m³). The liquid-liquid interfacial tension has been determined with the pending droplet method to 35 ± 2 dynes/cm. The ratio of the filling heights SOIL/WSS was 8.4/1.6. The choice of heights was made in order to obtain a variety of different patterns, including a transition from squares to hexagons [18]. The sugar concentration has been adapted to match the refractive index to that of the covering silicone oil ($n \simeq 1.405$) to a precision of 5×10^{-4} . The Ni²⁺-ions produce a broad absorption band in the spectral region 600-800 nm and provide high contrast patterns projected onto the diffusive screen. The container is illuminated from below with parallel light, and a band pass filter in front of the camera was used to detect only wavelengths $\lambda = (655 \pm 5)$ nm. By varying the intensity of the lamp the flat interface has been set to a level of about 50% of the maximum optical transmission. At a NiSO₄ concentration of 17% by weight the contrast between the light intensity passing through crests and valleys of the wave pattern was optimum. The associated coefficient of optical absorption was measured as $\alpha = 5.2 \pm 0.1$ cm⁻¹. In order to avoid uncontrolled changes of the viscosity, density and interfacial tension of both liquids all the measurements were performed at a constant temperature ($23 \pm 0.1^\circ$ C). The Faraday waves were excited by an electromagnetic shaker vibrating vertically with an acceleration in the form $a(t) = a_0 \cos(\Omega t)$. The driving signal came from a computer via a D/A-converter and the acceleration has been measured by piezoelectric sensor. A self developed closed-loop algorithm was used to suppress higher harmonics $n(\Omega t)$ in the driving signal to guarantee a purely harmonic driving. Faraday patterns were recorded in the following way: a high speed (250 Hz) 8-bit CCD camera was mounted some distance above the diffusive screen. Pictures were taken synchronous to the external driving. For a certain instant t_o the surface elevation of the Faraday patterns $h(x, y, t_o)$ is given by:

$$h(x, y, t_o) = \frac{1}{\alpha} \ln \frac{I_r(x, y)}{I_p(x, y, t_o)} \quad (1)$$

where $I_r(x, y)$ and $I_p(x, y, t_o)$ are 2D intensity distributions captured by the camera for the reference picture (flat interface, $a_o = 0$) and for the Faraday pattern ($a_o \neq 0$), respectively. Finally, the surface elevation function $h(x, y, t)$ are Fourier transformed and the time evolution of the Fourier amplitudes and phases of spatial modes is extracted. The use of a high speed camera compared to the earlier measurements by some of the co-authors [2] allows for a better temporal resolution and the

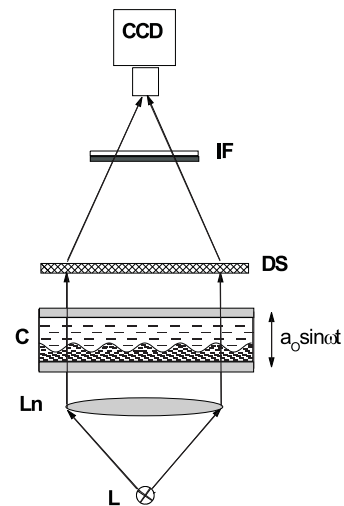


FIG. 1: Experimental setup: L - halogen lamp, Ln - lens, C - container filled by two liquids: SOIL and WSS with the same refractive indices, DS - diffusive screen, IF - interference filter, CCD - high speed CCD camera.

method is not sensitive to distortions (defects) on time scales of several periods. The logarithm of the intensity profile renders the dynamic range nonlinear, and with an 8-bit dynamical range the resolution is approximately 1% (2%) at small (high) surface elevations, relative to the maximal surface heights. The validity of the method has been also checked with flat layers of colored liquids of different thicknesses and the same accuracy was found. However, one should note that the Fourier transformation integrates over many pixels and a significant better resolution is to expect.

3. The linear regime

The experiments have been performed by quasistatically ramping the driving amplitude for the frequencies $f = \Omega/2\pi = 12, 16, 20, 29$ and 57 Hz from slightly below the critical acceleration a_c ($\varepsilon = (a - a_c)/a_c = -0.02$) up to just below the acceleration where the interface disintegrates and droplets form. In the same form a ramp was driven down to check for hysteretic effects, of which none were found. For each amplitude step a series of pictures were taken and Fourier transformed. Typically the pattern occurs in the center region of the container first but evolves in a range of $\Delta\varepsilon = 0.02$. From the Fourier transformation of the pictures at $-0.02 < \varepsilon < 0.1$ (Fig. 5) the critical acceleration a_c and the critical wavenumber k_c has been determined (Fig. 2). The experimental data can be compared with the results from the theoretical linear stability analysis that has been performed using the algorithm proposed by Kumar and Tuckerman[3]. The agreement between theory and experiment is very good, similar to former studies at the liquid-air interface [19, 20]. But with our new technique we are now able to

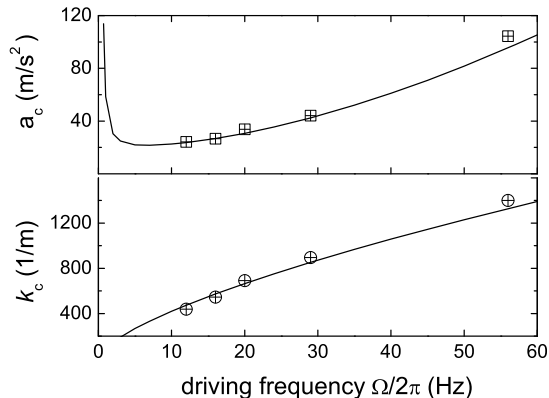


FIG. 2: Critical acceleration a_c and critical wave number k_c for different driving frequencies Ω . The symbols mark experimental data, the lines the theoretical linear stability analysis. The size of the symbols coincide with the size of the error bars.

verify more details of the predictions of the linear theory, e.g. the temporal spectra at onset of the instability. It is a particular feature of the Faraday-Experiment, that at onset only one wave number k_c becomes unstable, but the temporal spectrum already contains multiples of the fundamental oscillation frequency ω at onset. We are in the regime of subharmonic response and the fundamental oscillation frequency at onset is always $\omega = \Omega/2$ but the spectrum also contains $(n + 1/2)\Omega$ frequency components. More precisely we can write the surface deformation $h(\mathbf{r}, t)$ as

$$h(\mathbf{r}, t) = \frac{1}{4} \sum_{i=1}^N (A_i e^{i\mathbf{k}_i \cdot \mathbf{r}} + c.c.) \sum_{n=-\infty}^{+\infty} \zeta_n e^{i(n+1/2)\Omega t} \quad (2)$$

Here $\mathbf{r} = (x, y)$ are the horizontal coordinates. The set of *complex* Fourier coefficients ζ_n are the components of the eigenvector related to the linear stability problem and determine the subharmonic time dependence. The spatial modes are characterized by the wave vectors \mathbf{k}_i , each carrying an individual *complex* amplitude A_i . These quantities are determined by the nonlinearities of the problem. In principle the \mathbf{k}_i can have any length and orientation but at onset the relation $|\mathbf{k}_i| = k_c$ holds. The number N of participating modes determines the degree of rotational symmetry of the pattern: $N = 1$ corresponds to lines, $N = 2$ to squares, $N = 3$ to hexagons or triangles, etc. It can be shown [22] that the ζ_n and ζ_{-n} are coupled in a way that $\zeta_n = \zeta_{-n}$ so that heterodyning of right and left travelling waves always result in *standing* waves.

Equation 1 then reads

$$h(\mathbf{r}, t) = \sum_{i=1}^N (|A_i| \cos \mathbf{k}_i \cdot \mathbf{r} + \phi_i) \times \sum_{n=0}^{+\infty} (|\zeta_n| \cos(n + 1/2)\Omega t + \psi_n) \quad (3)$$

The complex eigenvectors ζ_n can be calculated modulo a constant factor and the ratio of the amplitudes $|\zeta_n|/|\zeta_{n+t}|$ as well as the temporal phases ψ_n can be compared with experimental data. They are obtained in the following way: For each step in the driving amplitude a series of snapshots of the surface state (Fig. 5) is taken. The primary pattern consists of squares and their formation is governed by the nonlinearities of the problem and one of our goals is to identify how far from onset the predictions from the linear theory hold.

An analysis of the Fourier transformation of the pictures yield amplitudes $A(t)(\mathbf{k}(ij))$ that are shown in Fig. 6. For the wave vectors $\mathbf{k}(ij)$ the nomenclature from crystallography is used, e.g. $\mathbf{k}(10)$ and $\mathbf{k}(01)$ are the vectors that generate the simple unit cell of the square pattern (Fig. 5). The temporal evolution of the amplitude of one of the critical modes $A(t)\mathbf{k}(10)$ with $|\mathbf{k}(10)| = k_c$ (Fig. 6 is then again Fourier transformed and a typical spectrum is shown in Fig. 7a). These data are taken for all driving strengths ε (Fig. 8a) and we always find the same values for $A(t)\mathbf{k}(10)$ and $A(t)\mathbf{k}(01)$ within the experimental resolution. In agreement with former investigations [15] in a system with a larger aspect ratio (container size to wave length) our study reveals also that the fundamental spatial mode $|\mathbf{k}(10)| = k_c$ for all ε . We can now extract the ratio of $A(\Omega/2, \mathbf{k}(10))/A(\Omega/2, \mathbf{k}(10))$ that is shown in the inset of Fig. 3. The contribution of higher harmonics is in the order of 5 to 10% and increases slightly with the driving strength. The agreement between the experimental data and the linear theory is again very good up to driving strength $\varepsilon > 0.5$, especially for lower driving frequencies. It is very surprising that the agreement even holds up to secondary patterned surface states, where a transition from a square to a hexagonal state has been taken place and, as we show later, strong nonlinear contributions participate in the dynamics of the system. The experimental data show also that at driving strength as low as $\varepsilon = 0.02$ the surface state consists of no measurable higher spatial Fourier modes (see Fig. 8) but of higher temporal harmonics in perfect agreement with the linear theory. This allows an extrapolation of $A(\Omega/2, \mathbf{k}(10))/A(\Omega/2, \mathbf{k}(10))$ to the neutral situation $\varepsilon = 0$ for all driving frequencies Ω (Fig. 3). The frequency ratio decreases first with increasing frequency and has a minimum at $\Omega/(2\pi) \approx 40Hz$. This characteristic shape reflects the amount of damping present in the system. At low driving frequencies the ration between fill height and wave number is small. In this regime damping from the bottom, that increases with decreasing frequency, is most significant. For larger

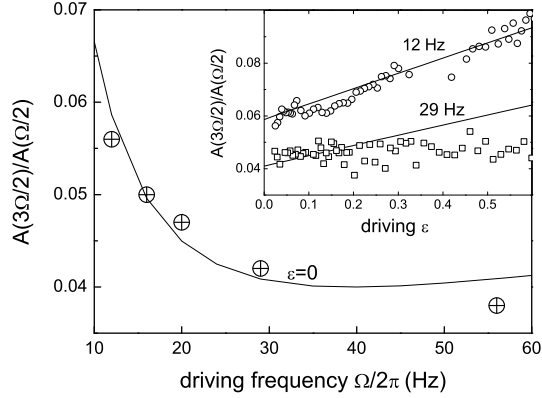


FIG. 3: The ratio of the amplitudes $A(3\Omega/2)/A(\Omega/2)$ of the $\mathbf{k}(10)$ mode at $\varepsilon = 0$ for different driving frequencies. The values are extrapolated from measurements at $\varepsilon > 0$ shown in the inset: the amplitude ratios at $\Omega/2\pi = 12Hz$ and $29Hz$ as a function of the driving strength ε .

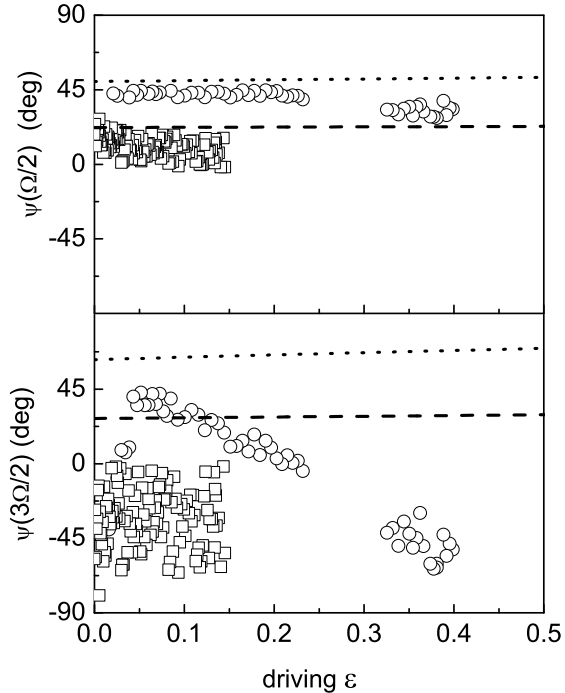


FIG. 4: The temporal phases $\psi(\Omega/2)$ and $\psi(3\Omega/2)$ of the $\mathbf{k}(10)$ mode for two driving frequencies versus driving strength ε . The symbols mark experimental, the lines theoretical data. Squares and broken line: $\Omega/2\pi = 57Hz$. Circles and dotted line: $\Omega/2\pi = 12Hz$; in the range $0.2 < \varepsilon < 0.28$ a transition from squares to hexagons takes place and in this disordered state an extraction of phases is not possible.

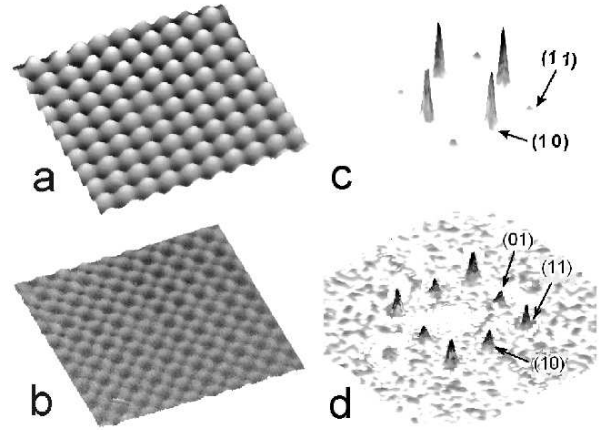


FIG. 5: Snapshots of the surface state and the power spectra at $\Omega/2\pi = 12Hz$ and $\varepsilon = 0.17$ ($a_0 = 30.0 \text{ m/s}^2$) for two different temporal phases a) at maximum and b) minimum surface elevation as indicated in Fig. 6

driving frequencies the damping from the bulk of the liquid (a function increasing with the frequency) is the strongest contribution. This behavior is also reflected in the critical accelerations (compare with Fig. 2). The ratio $A(\Omega/2, \mathbf{k}(10))/A(\Omega/2, \mathbf{k}(10))$ has been evaluated too, but the experimental resolution is not sufficient here for a conclusive comparison between theory and experiment.

In the same way the temporal phases ψ_n can be extracted from the Fourier spectrum and once more a good agreement between the theoretical predictions and experimental data is obtained, at least for the fundamental $\Omega/2$ component. For the $3\Omega/2$ component the scatter of the experimental data is very large and we find significant differences between experiment and theory. But besides the large scatter we observe a pronounced nonmonotonic behavior of the $\psi_{3/2\Omega}$ component at $57Hz$ and this part of the spectrum seems to be governed by nonlinear interactions.

4. The nonlinear surface state at $\Omega = 12Hz$

A. The square state

The primary pattern near onset ($0 < \varepsilon < 0.28$) consists of squares, shown in Fig. 5. Their formation is determined by the minimum of the Lyapunov functional of the according amplitude equation of the critical modes [21] and a quantitative theoretical prediction of the expected pattern can be given by inspection of the cubic coupling coefficient [4]. To our knowledge, for a two liquid system there has not yet been an attempt to calculate this coefficient, but squares are a common pattern in free surface experiments with low viscous liquids. The am-

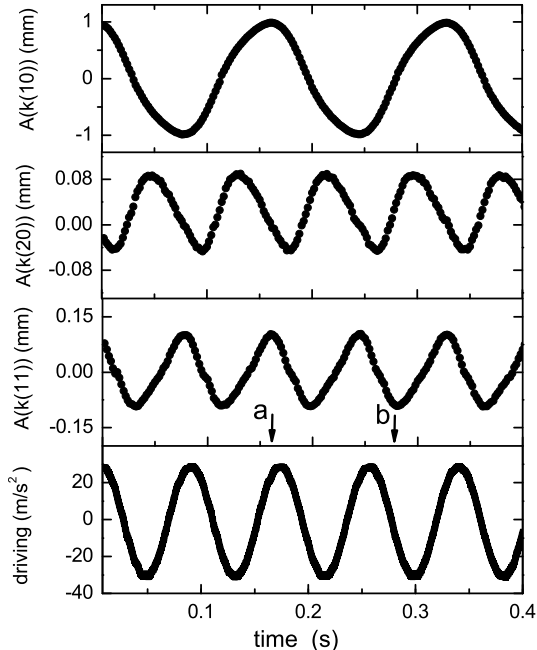


FIG. 6: The absolute amplitudes A of different spatial modes and the driving signal $a(t)$ in the square state at $\Omega/2\pi = 12\text{Hz}$ and $\varepsilon = 0.17$ ($a_0 = 30.0 \text{ m/s}^2$). Please note that unlike in Ref. [2] not the square root of the power spectra but the amplitude A of a deformation $h(\mathbf{r}, t) = A\cos(\mathbf{k}(ij) \cdot \mathbf{r})$ is shown.

plitude equations follow from a solvability condition of a weakly nonlinear analysis of the underlying constitutive equation, and its principal form is determined by the symmetries of the system. For the subharmonic response one can write

$$\tau \partial_t A(\mathbf{k}_i) = \varepsilon A(\mathbf{k}_i) - \sum_{j=1}^N \Gamma(\theta_{ij}) |A(\mathbf{k}_j)|^2 A(\mathbf{k}_i), \quad (4)$$

with τ the linear relaxation time and $\Gamma(\theta_{ij})$ the cubic coupling coefficient that depends on the angle θ_{ij} between the modes \mathbf{k}_j and \mathbf{k}_j with $|\mathbf{k}_{i,j}| = k_c$. The amplitudes $A(\mathbf{k}_i)$ are modulated with a subharmonic $(n+1/2)\Omega$ time spectrum given by the ζ_n from the linear eigenvectors. Equation 4 predicts a pitchfork bifurcation and in order to study this scenario one has to extract the different temporal Fourier modes of the measured $A(\mathbf{k}_i, t)$ (Fig. 6) first. The result is shown in Figs. 7 and 8a. As long as the pattern consists of squares there are no harmonic time dependencies in the basic spatial modes to observe, but a continued growth of $\Omega/2$ and $3\Omega/2$ contributions. The $5\Omega/2$ contribution is very weak and only slightly larger than the noise. The square of the sum of the amplitudes $A_s = A(\Omega/2) + A(3\Omega/2)$ yields a straight line if plotted versus the driving strength ε (Fig. 8c) as one would expect for the case of a pitchfork bifurcation. From the

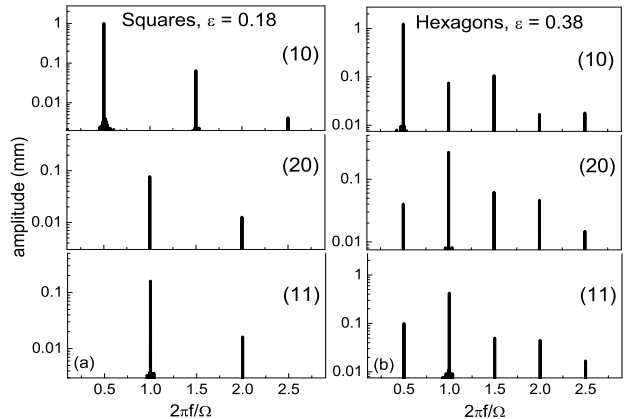


FIG. 7: The temporal spectra of the amplitudes $A(\mathbf{k}(ij, \omega))$ of different spatial modes at $\Omega/2\pi = 12\text{Hz}$ and a driving strength: a) $\varepsilon=0.18$ in the square state and b) $\varepsilon=0.38$ in the hexagonal state.

slope we can extract the cubic coupling coefficient $A_s = \varepsilon/\Gamma(90^\circ)$, and we find $\Gamma(90^\circ) = 0.179\text{mm}^{-2}$.

Now we can inspect the next higher harmonic spatial modes $A(\mathbf{k}(11))$ and $A(\mathbf{k}(20))$. Their temporal evolution is shown in Fig. 6. Both modes are a result of an interaction of two fundamental modes, $\mathbf{k}(11) = \mathbf{k}(10) + \mathbf{k}(01)$ and $\mathbf{k}(20) = \mathbf{k}(10) + \mathbf{k}(10)$. Quadratic coupling does not appear in the amplitude equations, but they are a natural consequence of nonlinear spatial wave interaction and it is no surprise that we find that they obey harmonic oscillations, shown in Fig. 7a. The striking result of our analysis is rather the constant offset that we find in the $A(\mathbf{k}(11))$ and $A(\mathbf{k}(20))$ spectrum (Fig. 6). This means that in addition to the oscillatory part, the interfacial profile is also composed of contributions of constant deformations of the form $h(\mathbf{r}, t) = |A_i|\cos\mathbf{k}_i \cdot \mathbf{r}$. This might surprisingly first, but please note that this does not violate the mass conservation. Actually, it is a simple consequence of the quadratic coupling of a *real* standing surface wave oscillation, $\Re(e^{i\mathbf{k}_i \cdot \mathbf{r}} e^{i\mathbf{k}_i \cdot \mathbf{r}} e^{i\Omega/2} e^{-i\Omega/2}) = \cos 2\mathbf{k}_i \cdot \mathbf{r} (1 + \cos\Omega)$ (compare also Fig. 14c).

This quadratic coupling scheme can be verified by plotting $A(\mathbf{k}(20))$ and $A(\mathbf{k}(11))$ versus the square of the amplitude of the fundamental mode $A(\mathbf{k}(10))$ or the product $A(\mathbf{k}(10)) \times A(\mathbf{k}(01))$ respectively. The data can be perfectly reproduced by a linear fit. From the slope one gets the strength of this nonlinear coupling and we do find the same values for all frequencies $\Omega/2\pi = 16, 20, 29 \text{ Hz}$ where squares are to be observed. Finally our Fourier analysis yields that the imaginary part of the coupling scheme obeys the same resonance conditions, and the spatial phase of the higher harmonic modes is given by $\phi(\mathbf{k}(20)) = 2\phi(\mathbf{k}(10))$ and $\phi(\mathbf{k}(10)) + \phi(\mathbf{k}(01))$.

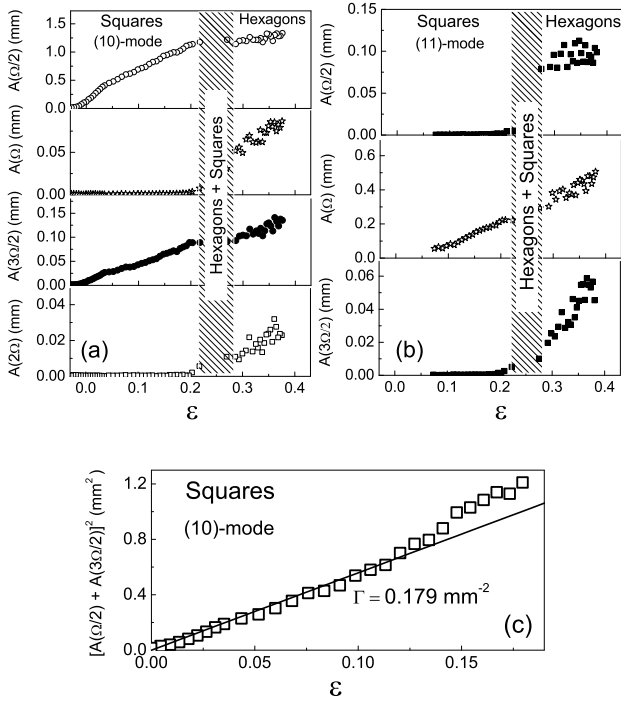


FIG. 8: The amplitudes $A(n/2\Omega)$ of the a) $\mathbf{k}(10)$ and b) $\mathbf{k}(11)$ mode at $\Omega/2\pi = 12Hz$ as a function of the driving strength ϵ . c): the square of the sum of the subharmonic components of the $A(10)$ mode versus ϵ . As expected for a forward bifurcation the data can be linearly fitted, at least up to driving strength of $\epsilon \approx 0.1$

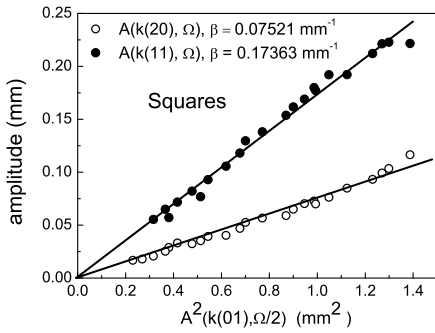


FIG. 9: The amplitudes $A(\mathbf{k}(20))$ and $A(\mathbf{k}(11))$ versus the square of the amplitude of the fundamental mode $A(\mathbf{k}(10))$ or the product of $A(\mathbf{k}(10))$ and $A(\mathbf{k}(01))$ respectively ($\Omega/2\pi = 12Hz$).

B. The hexagonal state

In the range ($0.20 < \epsilon < 0.28$) the pattern becomes disordered and transforms at higher driving strength to a hexagonal state (see Fig. 10) that consists of three fundamental spatial Fourier modes $\mathbf{k}_{1,2,3}$. But please note that for the construction of the crystallographic simple

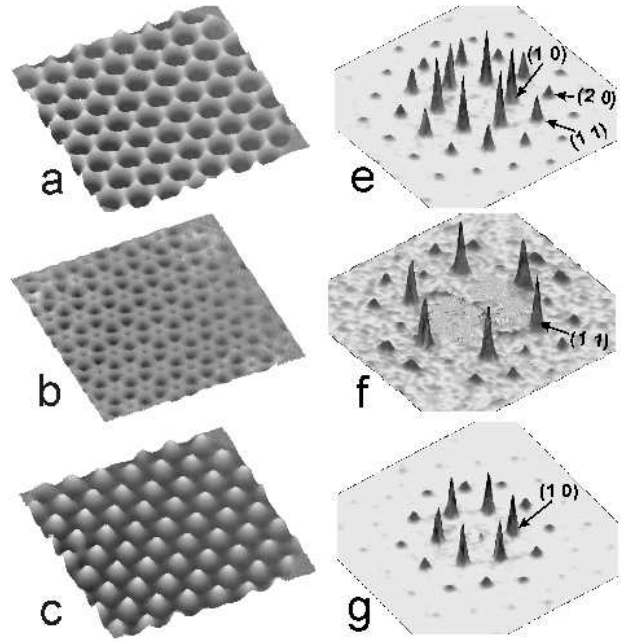


FIG. 10: Snapshots of the surface state and the Power spectra at $\Omega/2\pi = 12Hz$ and $\epsilon = 0.37$ ($a_0 = 39.3$ m/s²) for three different temporal phases. a) down hexagons, b) minimal surface elevation, c) up hexagons. See Refs. [2, 12] for further explanations on the switch from up to down hexagons in the Faraday-Experiment.

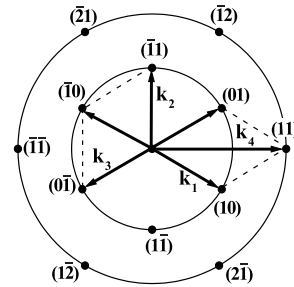


FIG. 11: Vector diagram of the interacting modes for the hexagonal surface state.

unit cell two vectors $\mathbf{k}(10) = \mathbf{k}_1$ and $\mathbf{k}(\bar{1}\bar{1}) = \mathbf{k}_2$ are sufficient ($\mathbf{k}(\bar{1}\bar{1}) + \mathbf{k}(10) = \mathbf{k}(0\bar{1}) = \mathbf{k}_3$, as indicated in Fig. 11).

An analysis of the temporal behavior of the amplitudes $A(\mathbf{k}(ij))$ of the spatial modes reveals, besides the the striking offset with the according constant spatial sinusoidal surface deformation, both harmonic and subharmonic time dependencies (see Fig. 7). While harmonic ($n\Omega$) temporal contributions in the higher spatial harmonics $\mathbf{k}(20, 11)$ appear in a similar manner to that of the square pattern, the resonance between $\mathbf{k}(10) + \mathbf{k}(0\bar{1}) =$

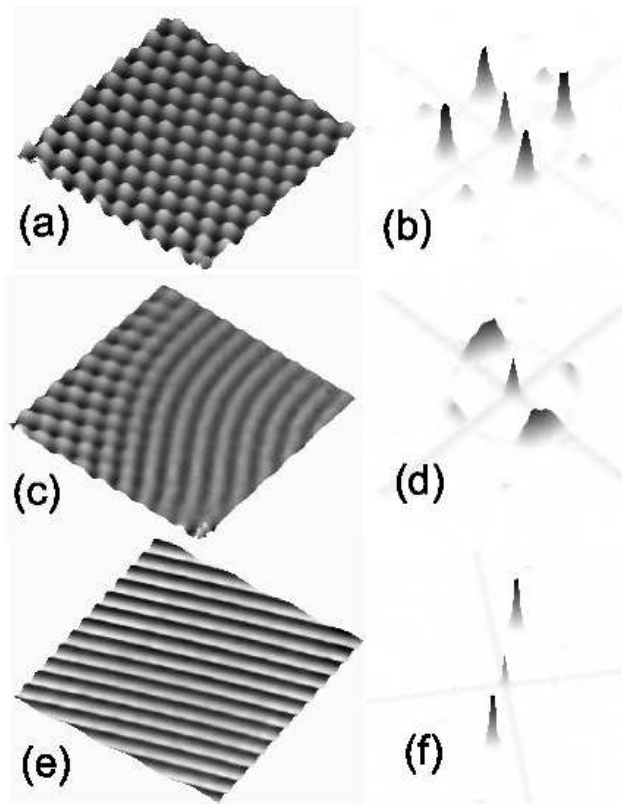


FIG. 12: Snapshots of the surface state and the power spectra at a,b) $\Omega/2\pi = 20\text{Hz}$, $\varepsilon = 0.6$ ($a_0 = 54.4 \text{ m/s}^2$) c,d) $\Omega/2\pi = 20\text{Hz}$, $\varepsilon = 0.08$ ($a_0 = 36.7 \text{ m/s}^2$) e,f) $\Omega/2\pi = 57\text{Hz}$, $\varepsilon = 0.11$ ($a_0 = 116.3 \text{ m/s}^2$).

$\mathbf{k}(1\bar{1})$ results in harmonic ($n\Omega$) contributions in the critical mode $|\mathbf{k}(1\bar{1})| = k_c$. Consequently the $n\Omega$ contributions couple with $(n + 1/2)\Omega$ contributions back into the spectrum of the $\mathbf{k}(20, 11)$ modes and result in subharmonic contributions. Harmonic contributions do not appear in the temporal spectra of the linear unstable modes k_c and quadratic interactions of $(n\Omega/2)$ components do not appear in the amplitude equations. Nevertheless the hexagonal state allows for a *spatial* resonance between linear unstable modes. In other words, this means that - within the framework of the weakly nonlinear approximation - we have here the interesting case where the system has a broken temporal symmetry that is driven by spatial resonances. It is not to be observed at any point in the quadratic state, where spatial resonances between linear unstable modes are forbidden too. This particular violation of the weakly nonlinear resonance conditions can best be seen in Fig. 8 where clearly the amplitudes of the Ω components of the $|\mathbf{k}(\mathbf{10})| = k_c$ mode grow from zero at the transition point from squares to hexagons, and similarly the $\Omega/2$ components of the $|\mathbf{k}(\mathbf{11})| = 2k_c$ modes.

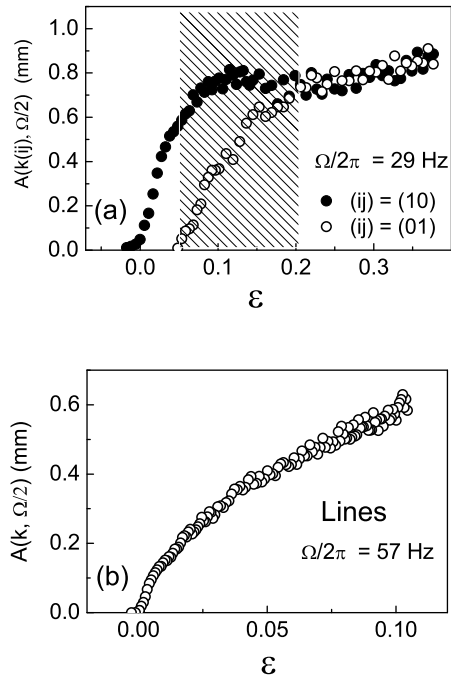


FIG. 13: The amplitudes $A(\Omega/2)$ of the a) $\mathbf{k}(10)$ and $\mathbf{k}(01)$ mode at $\Omega/2\pi = 29\text{Hz}$ and b) $\mathbf{k}(1)$ mode at $\Omega/2\pi = 57\text{Hz}$ as a function of the driving strength ε . The shaded region in a) indicates the crossed rolls state.

5. Pattern dynamics at $\Omega/2\pi > 12\text{Hz}$

The pattern dynamics at driving frequencies $\Omega/2\pi > 12\text{Hz}$ are characterized by a transition to lines. At $\Omega/2\pi = 16\text{Hz}$ the pattern still consists only of squares, while at $\Omega/2\pi = 20$ and 29Hz the primary pattern consists of (slightly distorted) lines (Fig. 12c,d). At higher driving strengths ε , a second Fourier mode perpendicular to the first one starts to grow (Fig. 13a) and the pattern evolves to a square state (Fig. 12a,b). For $\Omega/2\pi = 57\text{Hz}$ a pure line state is stable for all driving strengths (Fig. 12e,f and 13b). The pronounced constant offset in the $A(2\mathbf{k}, t)$ (Fig. 14b) mode is now larger than the temporal oscillation period and $A(2\mathbf{k}, t)$ never crosses the zero line. Similar like for the $A(\mathbf{k}20, \Omega)$ or $A(\mathbf{k}11, \Omega)$ modes in the squares state this quadratic coupling scheme holds also for the zero frequency modes as shown in (Fig. 14c).

6. Conclusion

We have demonstrated a new technique to measure quantitatively the spatio-temporal Fourier spectrum of Faraday waves on a two liquid interface. With this technique it is now possible to test theoretical predictions, especially those from numerical simulations. To our knowledge there are still no full Navier Stokes numerical simu-

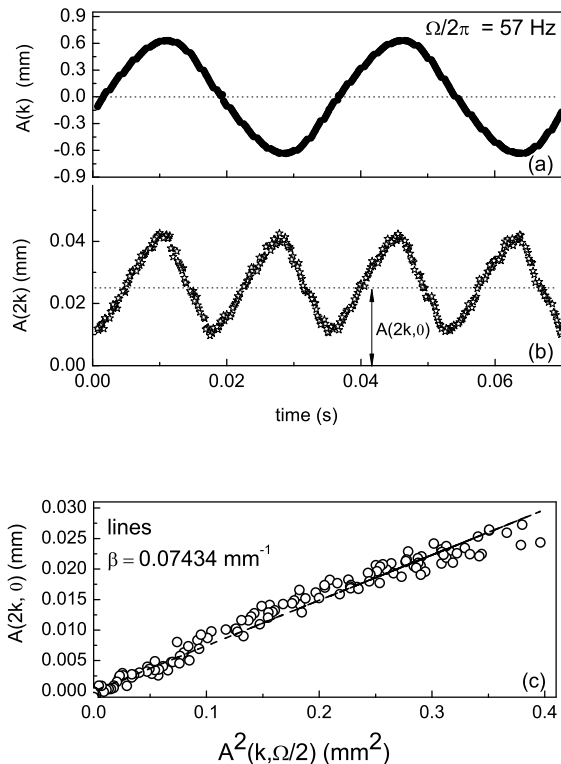


FIG. 14: a,b): The absolute amplitudes A of different spatial modes in the line state at $\Omega/2\pi = 57\text{Hz}$ and $\varepsilon = 0.11$ ($a_0 = 116.3 \text{ m/s}^2$). In b) the temporal constant offset $A(2k, 0)$ is indicated by the dotted line. c) The amplitude $A(2k, 0)$ versus $A^2(k, \Omega/2)$

lation of the 3D problem and quantitative tests for future work are most important. In this sense we would like to encourage such attempts. But with our technique we are also able to verify known predictions from the linear stability analysis and we find good agreement up to high driving strength of $\varepsilon \approx 0.5$. In the nonlinear state the most pronounced result is the identification of strong temporal constant sinusoidal surface deformations in the spectrum. And with our possibility to access any Fourier component separately we can identify several resonance mechanisms, including an interesting case of a temporal resonance violation by use of spatial resonances.

Acknowledgments

This work was supported by the German Science Foundation project Mu 912.

-
- [1] M. Faraday, Phil. Trans. Roy. Soc. Lond. **52**, 319 (1831).
 - [2] A. Kityk, H.W. Müller, K. Knorr, C. Wagner, Eur. Phys. Lett. **65**, 857 (2004).
 - [3] K. Kumar, L. S. Tuckerman, J. Fluid Mech. **279**, 49 (1994).
 - [4] W. Zhang, J. Viñals, J. Fluid. Mech. **336**, 301 (1997). P. Chen, J. Viñals, Phys. Rev. E **60**, 559 (1999).
 - [5] for a review see: J. W. Miles and D. Henderson, Ann. Rev. Fluid Mech. **22**, 143 (1990); H. W. Müller, R. Friedrich, and D. Papathanassiou, *Theoretical and experimental studies of the Faraday instability*, in: *Lecture notes in Physics*, ed. by F. Busse and S. C. Müller, Springer (1998).
 - [6] S. T. Milner, J. Fluid Mech. **225**, 81 (1990);
 - [7] B. Christiansen, P. Alstrom, Phys. Rev. Lett. **68**, 2157 (1992).
 - [8] W. S. Edwards, S. Fauve, J. Fluid Mech. **278**, 123 (1994).
 - [9] D. Binks and W. van de Water, Phys. Rev. Lett. **78**, 4043 (1997).
 - [10] A. Kudrolli and J. P. Gollub, Physica D **97**, 133 (1997).
 - [11] C. Wagner, H. W. Müller, and K. Knorr, Phys. Rev. Lett. **83**, 308 (1999).
 - [12] C. Wagner, H. W. Müller, and K. Knorr, Phys. Rev. E, **62**, R33 (2000).
 - [13] A. Kudrolli, B. Pier, and J. P. Gollub, Physica **123**, 99(1998);
 - [14] H. Arbell and J. Fineberg, Phys. Rev. Lett. **81**, 4384 (1998).
 - [15] A. Wernet, C. Wagner, D. Papathanassiou D., H.W. Müller, K. Knorr, Phys. Rev. E **63** 036305 (2001).
 - [16] R. Richter, J. Blasing, Rev. Sc. Instr. **72** 1729 (2001).
 - [17] W. B. Wright, R. Budakian, and S. J. Putterman, Phys. Rev. Lett. **76**, 4528 (1996).
 - [18] D. Binks and M.-T. Westra and W. van de Water, Phys. Rev. Lett. **79**, 5010 (1997).
 - [19] J. Bechhoefer, V. Ego, S. Manneville, and B. Johnson, J. Fluid Mech. **288**, 325 (1995).
 - [20] C. Wagner, H. W. Müller, and K. Knorr, Phys. Rev. Lett. **78**, 2357 (1997).
 - [21] M.C. Cross and P.C. Hohenberg, Reviews of Modern Physics **65**, 851 (1993).
 - [22] S. Douady, S. Fauve, Eur. Phys. Lett. **10**, 309 (1989).